Nanoscale Architecture of the Axon Initial Segment Reveals an Organized and Robust Scaffold

Christophe Leterrier, Jean Potier, Ghislaine Caillol, Claire Debarnot, Fanny Rueda boroni, Bénédicte Dargent

Article

Cell Reports

Nanoscale Architecture of the Axon Initial Segment Reveals an Organized and Robust Scaffold

Graphical Abstract

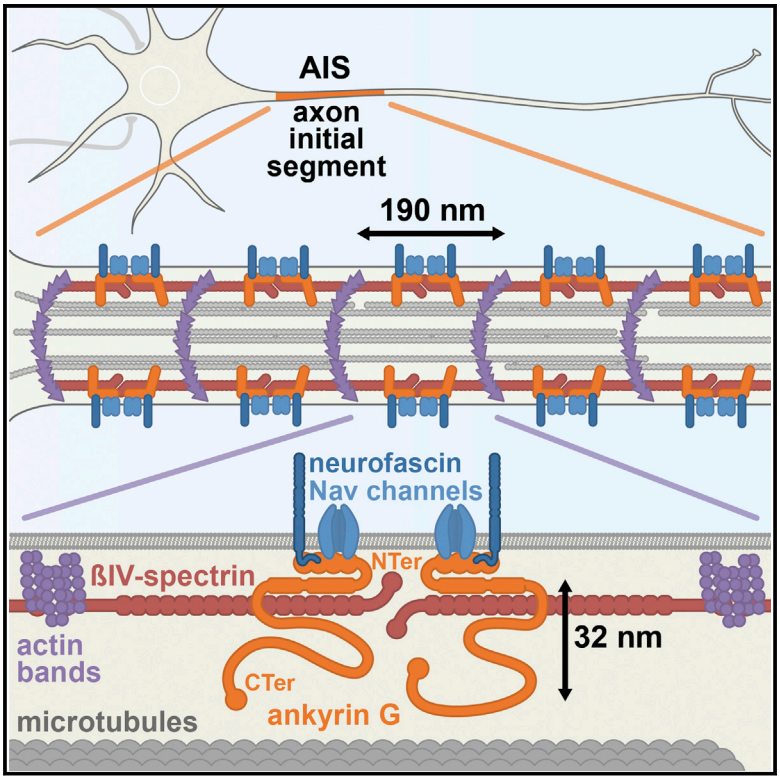

Authors

Christophe Leterrier, Jean Potier, Ghislaine Caillol, Claire Debarnot, Fanny Rueda Boroni, Bénédicte Dargent

Correspondence

christophe.leterrier@univ-amu.fr

In Brief

To understand how the axon initial segment (AIS) can control neuronal excitability and maintain axonal identity, it is crucial to know how its components are arranged at the molecular level. Using super-resolution microscopy, Leterrier et al. reveal the highly organized and robust nature of the AIS architecture.

Highlights

- The AIS nanoscale architecture was determined with super-resolution microscopy
- Head-to-head ßIV-spectrins connect actin rings to form a periodic submembrane complex
- Ankyrin G C-terminal tail extends ~30 nm below the submembrane complex
- This organized architecture is resistant to cytoskeleton perturbations

Leterrier et al., 2015, Cell Reports *13*, 2781–2793
December 29, 2015
http://dx.doi.org/10.1016/j.celrep.2015.11.051

CellPress

Cell Reports
Article

Nanoscale Architecture of the Axon Initial Segment Reveals an Organized and Robust Scaffold

Christophe Leterrier,[1,*] Jean Potier,[1] Ghislaine Caillol,[1] Claire Debarnot,[1] Fanny Rueda Boroni,[1] and Bénédicte Dargent[1]
[1]Aix Marseille Université, CNRS, CRN2M UMR7286, 13344 Cedex 15 Marseille, France
*Correspondence: christophe.leterrier@univ-amu.fr
http://dx.doi.org/10.1016/j.celrep.2015.11.051

SUMMARY

The axon initial segment (AIS), located within the first 30 μm of the axon, has two essential roles in generating action potentials and maintaining axonal identity. AIS assembly depends on a βIV-spectrin/ankyrin G scaffold, but its macromolecular arrangement is not well understood. Here, we quantitatively determined the AIS nanoscale architecture by using stochastic optical reconstruction microscopy (STORM). First, we directly demonstrate that the 190-nm periodicity of the AIS submembrane lattice results from longitudinal, head-to-head βIV-spectrin molecules connecting actin rings. Using multicolor 3D-STORM, we resolve the nanoscale organization of ankyrin G: its amino terminus associates with the submembrane lattice, whereas the C terminus radially extends (~32 nm on average) toward the cytosol. This AIS nano-architecture is highly resistant to cytoskeletal perturbations, indicating its role in structural stabilization. Our findings provide a comprehensive view of AIS molecular architecture and will help reveal the crucial physiological functions of this compartment.

INTRODUCTION

The directional flow of information in the brain is ensured by the cellular asymmetry of the neuron: the neuronal cell body receives synaptic inputs, and the axon propagates the action potential to downstream neurons. Neuronal asymmetry is maintained for years or even decades by a combination of passive (barriers) and active (directed traffic) processes, but the underpinning mechanisms remain largely unknown (Kapitein and Hoogenraad, 2011). Located along the first 20 to 40 μm of the axon, the axon initial segment (AIS) materializes the separation between the cell body and the axon. This location allows for the two main cellular functions of the AIS: the initiation of action potentials and the maintenance of axonal identity (Leterrier and Dargent, 2014).

The AIS ensures the proper generation of action potentials by concentrating voltage-gated sodium (Nav) and potassium (Kv7) channels at its surface. Together with specific cell adhesion molecules (CAMs) such as 186-kDa neurofascin, these channels are anchored by an interaction with the specialized AIS scaffold protein ankyrin G (ankG). AnkG also binds to a submembrane complex of βIV-spectrin and actin (for reviews, see Bennett and Lorenzo, 2013; Grubb and Burrone, 2010a; Leterrier and Dargent, 2014; Normand and Rasband, 2015). Furthermore, ankG links the AIS scaffold to microtubule fascicles via an interaction with end-binding proteins EB1 and EB3 (Leterrier et al., 2011). AnkG is the AIS master organizer: depletion of ankG results in the absence or disassembly of the whole AIS complex (Hedstrom et al., 2007, 2008; Jenkins and Bennett, 2001). In ankG-depleted neurons that lack an AIS, somatodendritic proteins progressively invade the proximal axon, resulting in the disappearance of microtubule fascicles and the formation of ectopic post-synapses (Hedstrom et al., 2008; Sobotzik et al., 2009): this demonstrates the role of the AIS for the maintenance of axonal identity.

Two proposed cellular processes contribute to this maintenance of axonal identity: a surface diffusion barrier that restricts the mobility of membrane proteins and lipids (Nakada et al., 2003; Winckler et al., 1999) and a traffic filter that could regulate intracellular diffusion and vesicular transport (Song et al., 2009). The underlying mechanisms are still mysterious, in particular the nature of the intracellular filter (Petersen et al., 2014; Watanabe et al., 2012). Our understanding of these processes depends on a better knowledge of the AIS architecture down to the molecular level. Super-resolution microscopy now allows us to observe macromolecular complexes in situ with a resolution down to a few tens of nanometers (Maglione and Sigrist, 2013) and has recently started to uncover the nanoscale organization of the AIS and axon. Stochastic optical reconstruction microscopy (STORM) has revealed that axonal actin is organized as submembrane rings periodically spaced every 190 nm (Xu et al., 2013), a result recently confirmed in living cells (D'Este et al., 2015). In the AIS, a periodic arrangement of actin, βIV-spectrin, and ankG is also detected (Zhong et al., 2014). However, the relative arrangement of AIS components resulting in this regular organization has not been directly addressed. Furthermore, although electron microscopy recently resolved individual ankG proteins as 150-nm-long rods (Jones et al., 2014), the nanoscale organization of this key protein within the AIS scaffold is still elusive. Notably, a connection between the plasma membrane components and intracellular structures by large isoforms of ankG has been proposed (Davis et al., 1996; Leterrier and Dargent, 2014) but remains hypothetical.

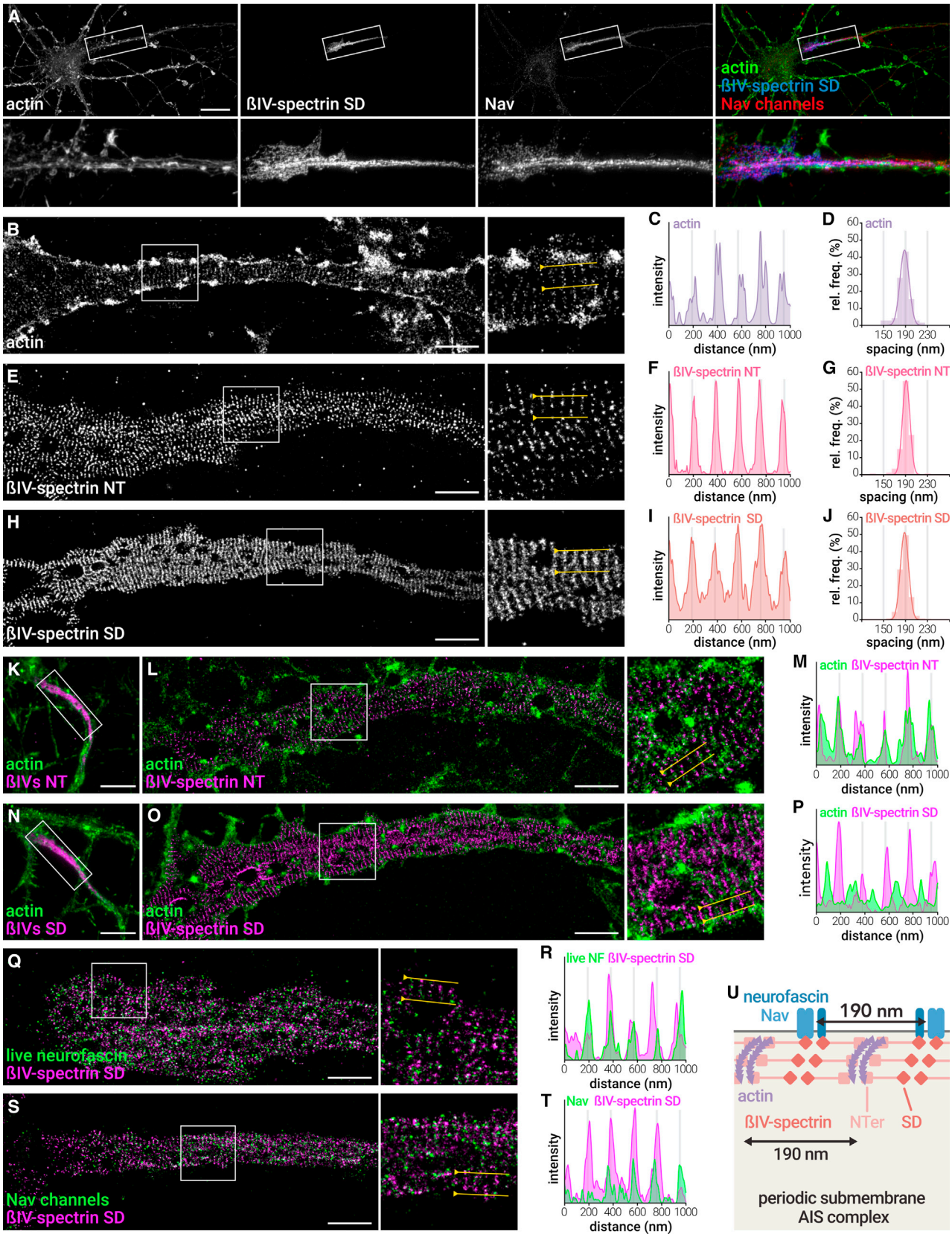

(legend on next page)

We set about quantitatively resolving the three-dimensional architecture of the AIS at the nanoscale level, in particular the arrangement of the master scaffold protein ankG. Multicolor 2D- and 3D-STORM of endogenous epitopes coupled to extensive quantification procedures allowed us to uncover the intricate ordering of the AIS scaffold. We directly demonstrate that the submembrane periodic lattice is composed of longitudinal head-to-head βIV-spectrin subunits connecting submembrane actin bands along the AIS. AnkG aminoterminal side is associated with this lattice, and its C-terminal side extends away from the plasma membrane, ~35 nm deeper in the cytoplasm. This could allow its interaction with peripheral microtubules, providing a structural basis for the regulation of vesicular entry into the axon. Finally, our observations reveal an unexpected robustness of the AIS scaffold: its ordered arrangement is resistant to pharmacological perturbations of the actin or microtubule cytoskeleton, and the radial extent of ankG even resists partial disassembly of the AIS induced by elevated intracellular calcium. This suggests that the nanoscale organization of AIS components is necessary for its integrity, and this structural robustness may support the AIS role as a gateway to the axon.

RESULTS

Actin and Longitudinal Head-to-Head βIV-Spectrin Subunits Form a Periodic Submembrane Complex at the AIS

To characterize the AIS nano-architecture, we first focused on the organization of the submembrane actin/βIV-spectrin complex. At the diffraction-limited level, actin was present, but not concentrated, in the AIS of mature neurons (15–21 days in vitro), in contrast to βIV-spectrin and Nav channels (Figure 1A). We used STORM that provided an ~17-nm lateral localization precision (see Figures S1A–S1C and Supplemental Experimental Procedures) to obtain images of the nanoscale actin organization. 2D-STORM images revealed the periodic arrangement of AIS actin as regular bands (Figures 1B and 1C), as described previously (D'Este et al., 2015; Xu et al., 2013). Line profiles obtained on STORM images exhibited intensity peaks with a regular spacing of ~190 nm (Figure 1D). We quantified the labeling periodicity by fitting sinusoids on 1-μm-long intensity profiles and fitting of the resulting spacing values histogram with a Gaussian curve (Figures S1D–S1G). The mean spacing and its spread were measured at 188 ± 8 nm for actin labeling along the AIS (Table S1). We next assessed the labeling obtained with anti-βIV-spectrin antibodies against either its aminoterminus (NT), which binds actin, or its specific domain (SD), close to the C terminus (CTer). Both βIV-spectrin NT (Figures 1E and 1F) and βIV-spectrin SD (Figures 1H and 1I) exhibited a strikingly periodic labeling pattern, and we measured the spacing distribution at 191 ± 7 nm for βIV-spectrin NT (Figure 1G) and 188 ± 8 nm for βIV-spectrin SD (Figure 1J), in close agreement with values reported previously (Xu et al., 2013; Zhong et al., 2014). As observed for actin by us and others (D'Este et al., 2015), AIS of large diameter showed a more-complex βIV-spectrin arrangement, with apposed stretches of bands resembling a herringbone parquet flooring (see Figure 2C for an example).

We next directly assessed the relative organization of actin and βIV-spectrin using two-color STORM of actin together with βIV-spectrin NT or SD (Figures 1K–1P). Although diffraction-limited level images were similar (Figures 1K and 1N), on STORM images, the periodic βIV-spectrin NT bands colocalized along actin bands (Figures 1L and 1M), whereas the βIV-spectrin SD bands were alternating with actin bands (Figures 1O and 1P). This differential position of βIV-spectrin ends relative to actin bands directly demonstrates the proposed model of head-to-head βIV-spectrin molecules connecting actin bands along the AIS (Figure 1U). Finally, we visualized the nanoscale distribution of two AIS membrane proteins shown to localize along the periodic submembrane complex, 186-kDa neurofascin (D'Este et al., 2015) and Nav channels (Xu et al., 2013). Single-color STORM images revealed a clustered organization of neurofascin and Nav channels, and we could detect the presence of some periodicity in the cluster arrangement (Figures S2A, S2B, S2D, and S2E), although it was quite low, resulting in flattened spacing histograms (190 ± 16 nm and 188 ± 18 nm for neurofascin and Nav channels, respectively). Two-color STORM revealed that the neurofascin and Nav clusters localized along βIV-spectrin SD bands, confirming their underlying periodicity (Figures 1Q–1T). Overall, our data validate and extend previous reports (D'Este et al., 2015; Xu et al., 2013; Zhong et al., 2014) and provide a comprehensive view for the molecular structure of the AIS submembrane complex (Figure 1U).

The AIS Submembrane Lattice Is Resistant to Actin Perturbation

The AIS scaffold is remarkably stable over time (Hedstrom et al., 2008). We wondered whether the βIV-spectrin periodic

Figure 1. Actin and Longitudinal Head-to-Head βIV-Spectrin Subunits Form a Periodic Submembrane Complex at the AIS

(A) Epifluorescence image of a neuron labeled for actin (phalloidin, green), βIV-spectrin SD (blue), and Nav channels (red). The scale bar represents 20 μm.
(B) STORM image of an AIS labeled for actin. The scale bars for (B), (E), (H), (L), (O), (Q), and (S) represent 2 μm.
(C) Intensity profile along the yellow line (gray lines are 190 nm apart).
(D) Histogram of the spacing values (n = 72 profiles from N = 3 independent experiments).
(E–G) Same as (B)–(D) for an AIS labeled for βIV-spectrin NT (histogram; n = 183; N = 3).
(H–J) Same as (B)–(D) for an AIS labeled for βIV-spectrin SD (histogram; n = 334; N = 11).
(K) Epifluorescence image of a neuron labeled for actin (green) and βIV-spectrin NT (magenta). The scale bars for (K) and (N) represent 10 μm.
(L and M) Two-color STORM image (L) of the AIS shown in (K); (M) corresponding intensity profile.
(N–P) Same as (K)–(M) for a neuron-labeled (green) and βIV-spectrin SD (magenta).
(Q and R) Two-color STORM image (Q) of an AIS labeled live for neurofascin (NF, green) and βIV-spectrin SD (magenta); (R) corresponding intensity profile.
(S and T) Same as (Q) and (R) for a neuron labeled for Nav channels (green) and βIV-spectrin SD (magenta).
(U) Structural model of the submembrane AIS complex.
See also Figures S1 and S2.

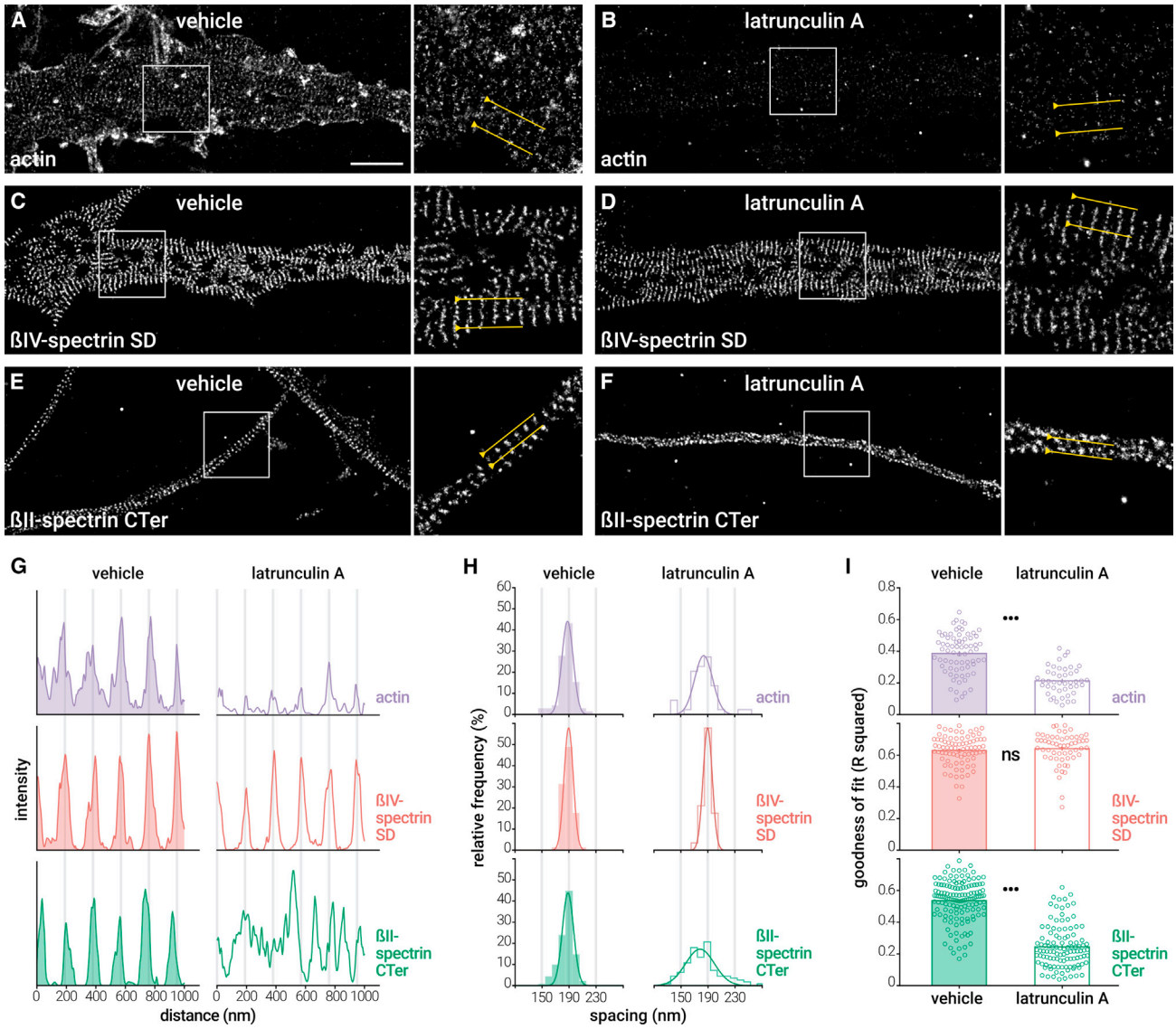

Figure 2. The AIS Submembrane Lattice Is Resistant to Actin Perturbation

(A–F) STORM images of neurons treated with vehicle (DMSO 0.1%; 1 hr; A, C, and E) or latrunculin A (latA; 5μM; 1 hr; B, D, and F), fixed and labeled for actin (AIS; A and B), ßIV-spectrin SD (AIS; C and D), or ßII-spectrin (distal axons; E and F). The scale bars for (A)–(F) represent 2 μm.

(G) Intensity profiles along the yellow lines in (A)–(F) for the actin (purple), ßIV-spectrin SD (red), and ßII-spectrin CTer (green) labeling. Intensities have been processed identically between the vehicle- (left) and latA- (right) -treated conditions.

(H) Histograms of the spacing values for each labeling (n = 44–143 profiles; N = 3 or 4).

(I) Goodness of sinusoid fit (R squared) for each labeling (n = 44–143; N = 3 or 4).

See also Figure S3.

lattice would nonetheless depend on integrity of the actin structure. To test this hypothesis, we assessed the ßIV-spectrin nanoscale distribution after actin depolymerization by latrunculin A (latA). Treatment with 5 μM latA for 1 hr disassembled actin filaments in all compartments, with a near disappearance of phalloidin labeling on diffraction-limited images and an 85% drop of labeling intensity at the AIS (Figures S3A–S3C). Notably, this short-term treatment did not affect the concentration of AIS components or the AIS length (Figures S3C and S3D).

STORM images revealed the disorganization of actin in the AIS, although a faint remnant of actin periodicity could still be detected, suggesting a selective resistance to depolymerization (Figures 2A, 2B, and 2G). Strikingly, the periodic pattern of the ßIV-spectrin SD was unaffected by latA treatment (Figures 2C, 2D, and 2G). In the control condition, actin and ßIV-spectrin in the AIS exhibited an identical spacing of 188 ± 8 nm (Figure 2H). After latA treatment, the spread of the spacing remained stable for ßIV-spectrin (190 ± 7 nm). Actin showed a significant drop in the goodness of sinusoid fit after latA treatment, indicating a

loss of periodicity (from 0.39 ± 0.02 to 0.21 ± 0.01; mean ± SEM), but the goodness of fit for βIV-spectrin remained high after actin depolymerization (0.63 ± 0.01 for vehicle; 0.64 ± 0.01 for latA; Figure 2I). Thus, periodic actin seems partially resistant to latA, and βIV-spectrin periodic organization in the AIS is resistant to actin perturbation.

To determine whether this robustness is specific to the AIS, we assessed the effect of actin disruption on the distal axon actin/spectrin complex, which forms a similar periodic structure with βII-spectrin instead of the AIS-specific βIV-spectrin (Xu et al., 2013). Using an antibody against the βII-spectrin CTer, we indeed found a highly periodic distribution along distal axons, with a regular spacing of 188 ± 8 nm (Figures 2E and 2G). βII-spectrin was still clustered after LatA treatment, but the regular spacing was disorganized, with a larger spacing spread (190 ± 22 nm; Figure 2H) and a drop of the R squared from 0.54 ± 0.01 to 0.25 ± 0.01 (Figure 2I), confirming previous results (Xu et al., 2013; Zhong et al., 2014). In conclusion, we found actin to be partially resistant to depolymerization in the AIS. In contrast to the actin/βII-spectrin complex found in the distal axon, the βIV-spectrin periodic lattice is completely resistant to actin perturbation by latA.

The ankG Spectrin-Binding Domain Associates with the Periodic Lattice, but Its CTer Part Is Not Periodically Arranged

What makes the actin/βIV-spectrin lattice in the AIS more resistant than the βII-spectrin/actin complex along the distal axon? Stabilization is likely due to the AIS master organizer ankG that recruits and maintains βIV-spectrin at the AIS (Yang et al., 2007). AnkG present at the AIS is a large 480-kDa protein, with a shorter 270-kDa isoform being also expressed (Bennett and Lorenzo, 2013; Jenkins et al., 2015). To characterize the nanoscale organization of ankG by STORM, we used antibodies directed against distinct domains of the protein (Figure 3A). A polyclonal antibody directed against a peptide epitope in the serine-rich domain (SR) was previously described (Bréchet et al., 2008), and we mapped the target domains of two monoclonal antibodies (anti-ankG clone 106/65 and 106/36) to the spectrin-binding (SB) and CTer domains, respectively (Figure S4A). We also used a tail480 antibody recognizing the distal part of the tail specific to 480-kDa ankG, close to the CTer (Figure S4B). These antibodies labeled the AIS of hippocampal neurons in a similar fashion at the diffraction-limited level (Figures 3B and 3C).

At the nanoscale level, we first localized the domain of ankG that interacts with βIV-spectrin (the SB domain) together with βIV-spectrin SD. Two-color STORM images showed that the ankG SB clusters localized along βIV-spectrin bands, resulting in correlated line profiles (Figures 3D and 3E). We next compared the periodicity of labeling for four different ankG domains: the SR domain (localized adjacent to the SB domain); the distal tail domain (tail480 antibody); or the CTer domain (formed by the last 300 residues of the protein; Figure 3A). On single-color STORM images, the regular spacing of ankG SB clusters was clearly detected (Figures 3G and 3H), as reflected by periodicity measurements (spacing 188 ± 13 nm; Figure 3I; Table S1). Periodicity was similar for the adjacent SR domain (Figures 3J and 3K), with a spacing of 188 ± 14 nm (Figure 3L). Both the distal tail and the CTer domain exhibited a clustered distribution, but periodic patterns were difficult to discern (Figures 3M, 3N, 3P, and 3Q), and the spacing histograms exhibited a significantly higher spread (182 ± 27 and 184 ± 20 nm for the distal tail and CTer, respectively; Figures 3O–3R). Accordingly, the goodness of sinusoid fit (R squared) dropped from 0.34 ± 0.01 for the ankG SB domain to 0.26 ± 0.01 for the SR, 0.20 ± 0.01 for the distal tail, and 0.22 ± 0.01 for the CTer domain (Table S1). This gradual loss of periodic distribution between the ankG SB and CTer domains validates and extends a recent observation (Zhong et al., 2014). In conclusion, ankG exhibits a periodic arrangement of its aminoterminal side that interacts with βIV-spectrin, but downstream domains, closer to its CTer, progressively lose this periodicity and become more disordered.

The ankG CTer Domain Extends Radially below the Submembrane Lattice

Why does the CTer part of ankG show a disorganized nanoscale distribution? We hypothesized it could extend away from the periodic submembrane lattice, deeper in the axoplasm, where it could reach intracellular partners (see Figure 4O). To test this, we resolved the transverse organization of the AIS using 3D-STORM, which attained an axial localization precision of ~33 nm (see Figures S5A–S5C and Supplemental Experimental Procedures). To map the radial position of AIS components, we performed two-color 3D-STORM with different epitopes co-labeled with βIV-spectrin SD as a reference (Figures 4A–4J). We first validated our method by imaging intracellular microtubules together with submembrane βIV-spectrin SD (Figure 4A). Although α-tubulin labeling was not resolved as continuous microtubules due to the fixation protocol used in these experiments (compare with Figure 5G), intracellular labeling was nevertheless clear on transverse sections and radial profiles, with the βIV-spectrin lattice encasing the α-tubulin labeling (Figures 4A and 4B). Next, we assessed the radial position of AIS membrane proteins: neurofascin using an antibody against an extracellular epitope (Figures 4C and 4D) and Nav channels using an antibody against an intracellular loop (Figures 4E and 4F). On YZ transverse sections, both neurofascin and Nav channels were found at the periphery of the βIV-spectrin submembrane lattice (Figures 4C and 4E), as confirmed by line profiles across transverse sections (Figures 4D and 4F).

We then assessed the transverse arrangement of ankG by imaging the two domains on opposite sides of the protein (SB and CTer domains), together with βIV-spectrin SD (Figures 4G–4J). The ankG SB domain colocalized with the submembrane βIV-spectrin lattice on transverse sections (Figures 4G and 4H). The ankG CTer domain was found to be more intracellular than βIV-spectrin: ankG CTer labeling was consistently found lining the intracellular side of the βIV-spectrin lattice (Figure 4I). On radial profiles, this resulted in the ankG CTer intensity peaks being shifted toward the axoplasm compared to the βIV-spectrin peaks (Figure 4J). As different AISs exhibit large variations in shapes (length, diameter, and roundness), we devised a method to precisely quantify the radial arrangement of epitopes independently of these variations. A Gaussian curve was fitted on radial profiles, and the distance between the Gaussian maxima for the

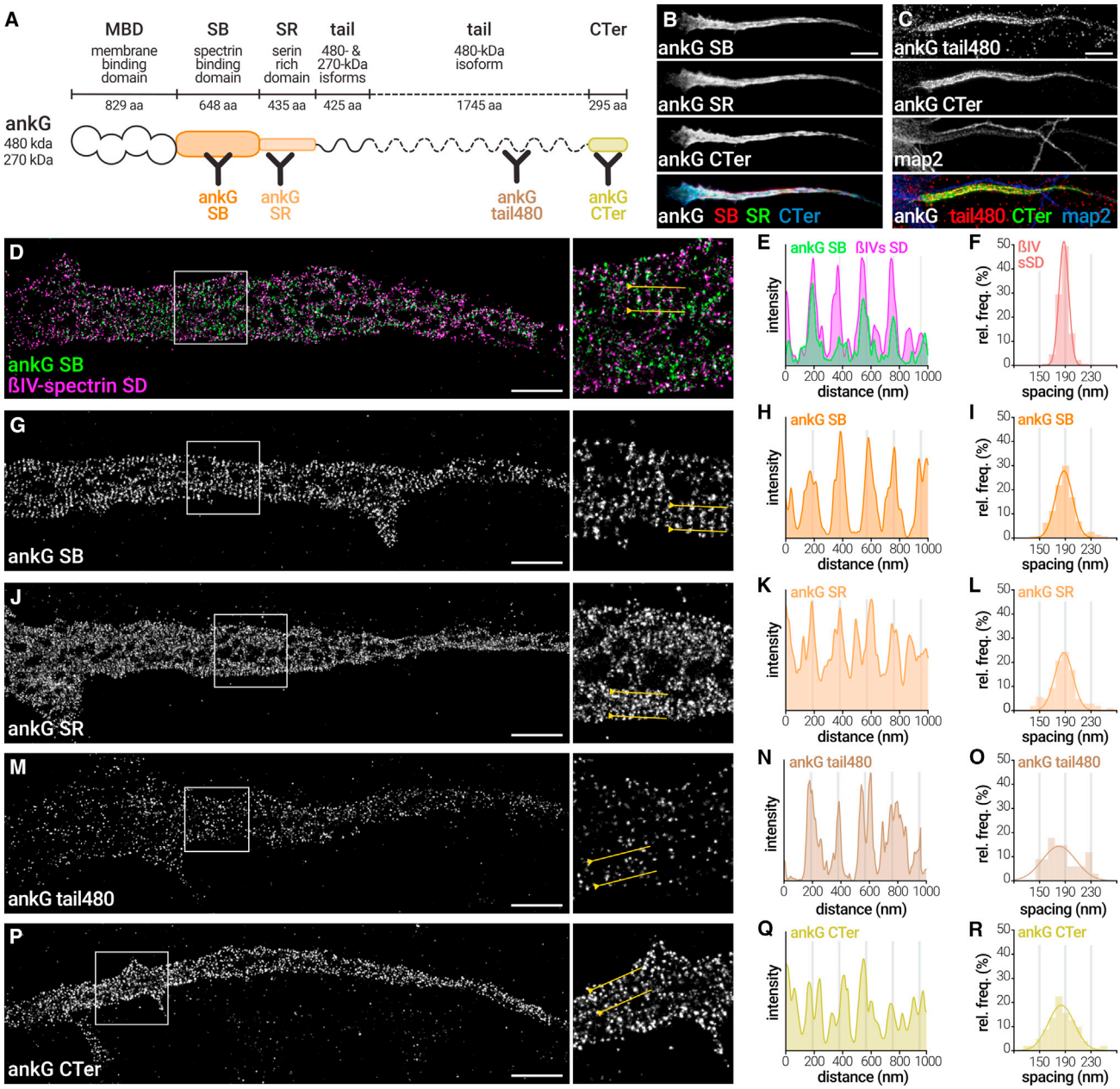

Figure 3. The ankG Spectrin-Binding Domain Associates with the Periodic Lattice, but Its CTer Part Is Not Periodically Arranged

(A) Cartoon of the ankG domains, with the target domains of the four anti-ankG antibodies used.

(B) Epifluorescence image showing the AIS of a neuron labeled for ankG SB (red), ankG SR (green), and ankG CTer (blue).

(C) Epifluorescence image showing the AIS of a neuron labeled for ankG tail480 (red), ankG CTer (green), and map2 (blue). The scale bars on (B) and (C) represent 5 μm.

(D) STORM image of an AIS labeled for ankG SB (green) and ßIV-spectrin SD (magenta). The scale bars for (D), (G), (J), (M), and (P) represent 2 μm.

(E) Intensity profiles for each channel along the yellow line.

(F) Histogram of the spacing values for the ßIV-spectrin SD labeling (same data as in Figure 1J).

(G–I) STORM image (G) of an AIS labeled for ankG SB; (H) corresponding intensity profile; (I) histogram of spacing values (n = 161 profiles; N = 6).

(J–L) Same as (G)–(I) for an AIS labeled for ankG SR (histogram; n = 107; N = 3).

(M–O) Same as (G)–(I) for an AIS labeled for ankG tail480 (histogram; n = 34; N = 2).

(P–R) Same as (G)–(I) for an AIS labeled for ankG CTer (histogram; n = 102; N = 4).

See also Figure S4.

two channels was measured, providing the distance value relative to the βIV-spectrin SD reference (Figures S5C–S5F). We determined the mean distance from the βIV-spectrin SD to the extracellular epitope of neurofascin to be 17 ± 1 nm and to the Nav intracellular loop to be 8 ± 1 nm (mean ± SEM; positive distance toward the axolemma; Figure 4M; Table S2). α-tubulin localization was broadly intracellular with a mean depth of −85 ± 4 nm (negative distance toward the axoplasm). The ankG SB domain was located just above βIV-spectrin, with a mean distance of 6 ± 1 nm. The CTer domain of ankG was significantly more intracellular, with a mean distance of −26 ± 1 nm to βIV-spectrin (Figure 4M). From these measurements, we determined ankG average radial extent: its CTer domain is on average 32 ± 1 nm deeper than its SB domain. We also mapped the position of the distal 480-kDa ankG tail relative to the ankG CTer (we could not use a βIV-spectrin SD reference due to antibody host species issues). The two epitopes were colocalized on YZ sections (Figures 4K and 4L), showing that the distal tail localizes at the same depth as the CTer, with a relative distance close to zero (−2 ± 2 nm; Figure 4N). In conclusion, we have showed that the AIS is organized transversally, with the ankG CTer extending below the submembrane complex toward the axoplasm (Figure 4O).

The Radial Extent of ankG Is Resistant to Actin or Microtubule Perturbation

AnkG can be considered as a scaffold linker that binds both to actin via βIV-spectrin and to microtubules via EB1/3 proteins (Leterrier et al., 2011). Thus, we wondered whether the ankG radial extent was dependent on the actin or microtubule cytoskeleton integrity. First, we used latA to acutely perturb actin and measured the radial distance between the ankG CTer domain and the βIV-spectrin SD. LatA treatment (5 μM; 1 hr) did not modify ankG arrangement: the ankG CTer domain was still found deeper than βIV-spectrin (Figures 5A–5D), with a distance of −26 ± 2 nm after treatment, compared to −24 ± 1 nm for vehicle (Figure 5E; Table S2). Thus, ankG radial extent does not depend on actin integrity.

Next, we used nocodazole at a high concentration (20 μM for 3 hr) to acutely perturb microtubules (Jaworski et al., 2009). At the diffraction-limited level, microtubules disassembly was observed after nocodazole treatment using an extraction/fixation procedure optimized for microtubule preservation (Figure S6A). A few filamentous structures were still brightly labeled, leading to a partial 55% decrease in labeling intensity at the AIS (Figure S6B). However, STORM imaging showed that these remaining microtubules were running along, but not inside the AIS, likely belonging to distal axons (Figures 5F–5I). In both vehicle- and nocodazole-treated neurons, periodicity measurement of the microtubule labeling along the AIS led to a flattened spacing histogram (190 ± 29 nm and 156 ± 32 nm, respectively) and low R-squared values (0.18 ± 0.09 and 0.17 ± 0.11, respectively), providing a baseline for our measurement procedure (Figures S6C–S6J).

AIS components were barely affected by the nocodazole treatment at the diffraction level (12% drop in ankG concentration; no significant change for βIV-spectrin or AIS length; Figures S6K–S6M). At the nanoscale level, the periodic βIV-spectrin lattice was not perturbed by nocodazole treatment (Figures S6N–S6S), with no change in spacing spread for the βIV-spectrin SD labeling (187 ± 8 nm for both vehicle and nocodazole; Figures S6P and S6S). This is in contrast with the partial disassembly of βII-spectrin rings recently observed after nocodazole treatment (Zhong et al., 2014), confirming the specific robustness of the AIS scaffold. Finally, we mapped the radial organization of ankG after nocodazole treatment (Figures 5J–5N). The localization of the ankG CTer domain was unaffected by nocodazole treatment: the ankG CTer domain distance to βIV-spectrin was −24 ± 1 nm for vehicle and −25 ± 1 nm for nocodazole (Figure 5N). The radial arrangement of ankG, as well as the longitudinal periodicity of the βIV-spectrin lattice, thus resists to actin filaments or microtubules perturbation.

Elevated K+ Partially Disassembles the AIS and Impairs the Periodic Lattice, but Not the ankG Radial Extent

To further probe the robustness of the AIS scaffold organization at the nanoscale, we used a treatment that would affect the AIS morphology without completely disassembling it. Increase in intracellular calcium concentration has been implicated in the AIS morphological plasticity (Grubb and Burrone, 2010b) and shown to trigger AIS disassembly in ischemic injury (Schafer et al., 2009). We incubated neurons in the presence of 45 mM KCl for 3 hr (Redmond et al., 2002) to acutely increase intracellular calcium concentration. First, we measured the effect of these treatments on the overall morphology of the AIS at the diffraction-limited level (Figures 6A and 6B): high KCl treatment resulted in partial disassembly of the AIS, with an ∼30% drop in βIV-spectrin and ankG-labeling intensity (Figure 6C) and a slight AIS shortening compared to the control condition (standard culture medium containing 5 mM KCl; Figure 6D). KCl treatment had a strong effect on the periodicity of the submembrane lattice (Figures 6E–6H), with the βIV-spectrin SD labeling exhibiting a flattened 189 ± 18-nm spacing distribution and a goodness of fit dropping from 0.58 ± 0.01 to 0.27 ± 0.01 (Figure 6I). In contrast, KCl treatments did not perturb the radial orientation of ankG (Figures 6J–6N), with an average distance of ankG CTer to βIV-spectrin SD at −24 ± 1 nm and −22 ± 2 nm for control and KCl treatments, respectively (Figure 6N). In conclusion, the range of perturbation performed (cytoskeleton and intracellular calcium) shows that the AIS nano-architecture is robust, with partial alterations appearing only when significant disassembly occurs for the whole AIS.

DISCUSSION

In this work, we have determined the nanoscale architecture of the AIS using super-resolution microscopy. STORM allowed us to quantitatively localize epitopes corresponding to known domains of AIS proteins and infer the precise arrangement of the AIS scaffold. First, we directly demonstrate that the previously described ∼190-nm periodic lattice along the AIS is formed by submembrane actin bands connected by longitudinal head-to-head βIV-spectrin subunits. Furthermore, we reveal the specific resistance of this actin/βIV-spectrin lattice against actin perturbation, compared to the βII-spectrin-based lattice found along the distal axon. We characterized the yet unknown arrangement

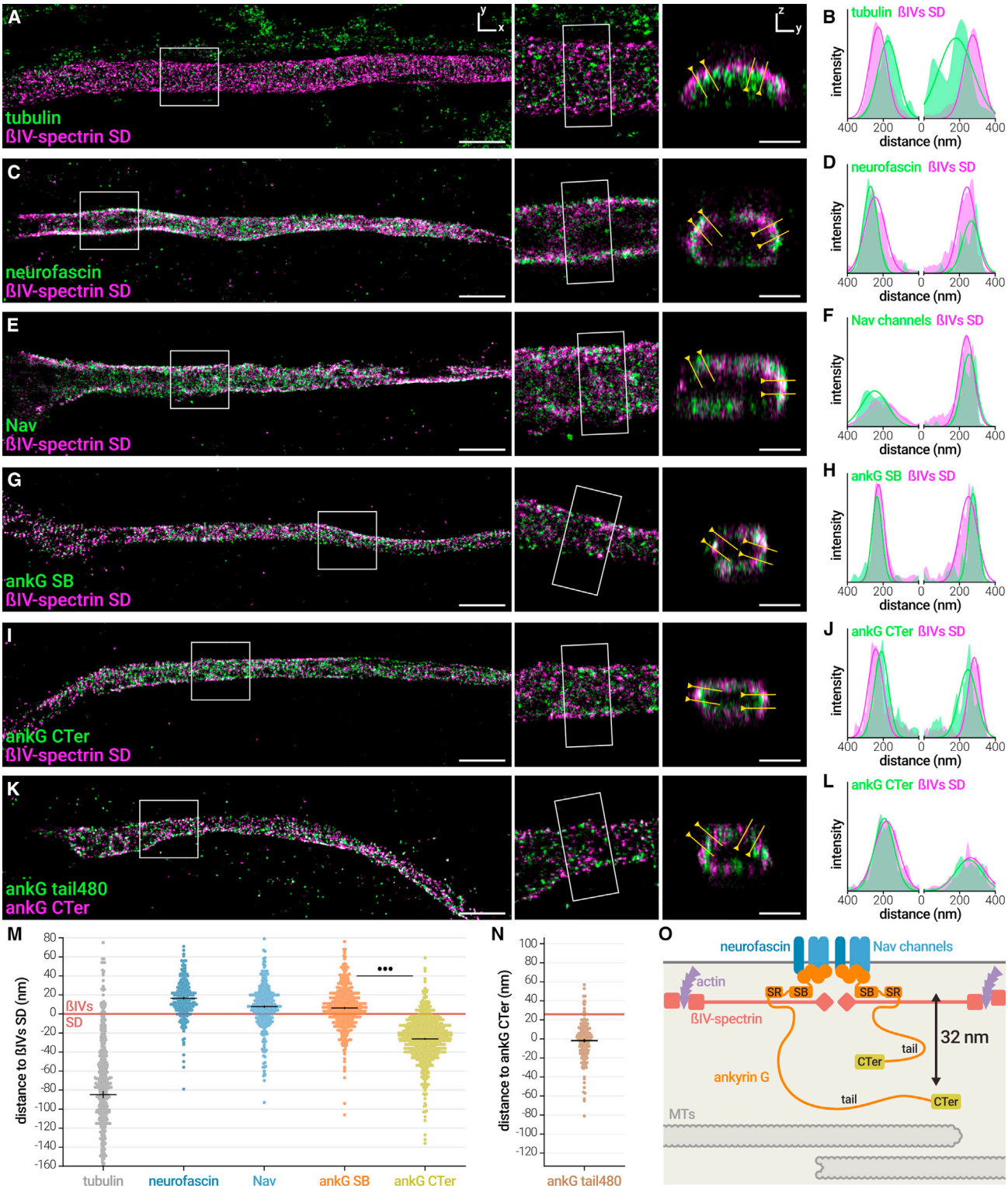

Figure 4. The ankG CTer Domain Extends Radially below the Submembrane Lattice

(A) 3D-STORM image of an AIS labeled for α-tubulin (green) and ßIV-spectrin SD (magenta).

(B) Intensity profiles for each channel (filled curves) and Gaussian fits used to calculate radial distances. For (A), (C), (E), (G), (I), and (K), profiles are taken along the yellow line on the corresponding transverse section shown; scale bars represent 2 μm for XY image and 500 nm for YZ section.

(C and D) Same as (A) and (B) for an AIS labeled for neurofascin (green) and ßIV-spectrin SD (magenta).

(legend continued on next page)

of the AIS master scaffolding protein ankG: the aminoterminal part of ankG associates with membrane proteins and βIV-spectrin in the submembrane lattice, resulting in a periodic distribution. In contrast, the CTer part does not exhibit this periodicity: we explain this by demonstrating that the CTer of ankG localizes deeper in the axoplasm, below the submembrane lattice. Thanks to 3D-STORM, we measured a 32-nm radial extent between ankG SB and CTer domains. Finally, we showed that the lattice periodicity, as well as the radial extent of ankG, is resistant to a range of perturbations, revealing that this nanoscale organization is a robust and structural feature of the AIS.

Longitudinal Organization: Periodic Submembrane Actin/βIV-Spectrin Lattice

The first striking feature of the AIS nano-architecture is the periodic arrangement of its submembrane scaffold. We observed a regular distribution of actin and βIV-spectrin extremities every ~190 nm along the AIS, confirming the periodic organization recently described (D'Este et al., 2015; Xu et al., 2013; Zhong et al., 2014). Purified brain spectrins have a length of ~195 nm (Bennett et al., 1982), suggesting a structural model where head-to-head βIV-spectrin subunits connect to actin bands at their NT extremities and to ankG/Nav channels complexes near their SD domain (Figure 1U). Using two-color STORM, we could detect correlated bands for actin/βIV-spectrin NT and anti-correlated ones for actin/βIV-spectrin SD, directly demonstrating the validity of this model. Interestingly, two isoforms of βIV-spectrin exist at the AIS: the 289-kDa βIV$\sum$1, and the ~160 kDa βIV$\sum$6 that lacks the aminoterminal part of βIV$\sum$1 (Lacas-Gervais et al., 2004; Uemoto et al., 2007). βIV$\sum$1 binds both actin and ankG and is likely to form the basis of the ~190-nm periodic lattice, in contrast to βIV$\sum$6, which does not bind actin. The detection of the two isoforms by the SD antibody could explain the higher localization counts and the larger individual bands compared to the NT antibody that only recognize βIV$\sum$1.

Recent work showed that a periodic lattice of βII-spectrin first appears along the whole axon, before being replaced at the AIS by βIV-spectrin in the mature neurons used in our study (Zhong et al., 2014). Furthermore, we found the AIS βIV-spectrin organization to be resistant to actin perturbation by latA (actin itself being partially stabilized at the AIS), as well as microtubule perturbation by nocodazole. It is likely that, in the AIS, the βIV-spectrin/actin complex is stabilized by the ankG/Nav channels complex. In the distal axon, the periodic βII-spectrin lattice does not depend on the presence of its ankyrin B partner (Lorenzo et al., 2014), and this could explain why it is sensitive to cytoskeleton perturbation (Zhong et al., 2014). Ankyrin B presence is rather required for βII-spectrin preferential concentration into the axon (Zhong et al., 2014), supporting a function in axonal transport rather than membrane structuration (Lorenzo et al., 2014).

Transverse Organization: Radial Extent of ankG

The second striking feature of the AIS nano-architecture is the radial arrangement of ankG. We demonstrate that the CTer part of ankG departs from the submembrane periodic lattice and is found deeper in the axoplasm. 3D-STORM and quantification of the radial distribution of epitopes allowed us to measure the radial extent of ankG, with a 32-nm average distance between the SB and CTer domains (see Figure 4M). It is unlikely that antibody penetration was an issue in our mapping of ankG organization, as we could visualize microtubules at deeper positions and throughout the entire transverse section of the AIS.

AnkG could stretch to hundreds of nanometers if its tail was fully extended, and it has been visualized as ~150-nm rods by scanning electron microscopy (Jones et al., 2014). The 32-nm radial extent value indicates that ankG actually lies in the vicinity of the plasma membrane and may adopt convoluted conformations in the scaffold. This limited radial extent could also be adopted by the shorter 270-kDa ankG isoform that lacks the distal 1,745 amino acids of the tail, as suggested by the similar depth measured using antibodies recognizing either the distal tail of 480-kDa ankG or the CTer domain shared by both isoforms. Interestingly, the proximal part of the 480-kDa ankG-specific tail (encompassing the S2417 residue) has recently been implicated in the recruitment of βIV-spectrin to the AIS (Jenkins et al., 2015), suggesting it could be located in the submembrane lattice. We found that the distal part of the tail (antibody targeting residues 3,516–3,530) as well as the CTer domain were located 25 nm deeper than βIV-spectrin: this suggests that the ankG distal tail is the part that exits the submembrane lattice. The insertion of the large exon coding for the SR and tail domains of neuronal ankG has thus led to an extension of ankG from the submembrane scaffold, potentially allowing the connection to more intracellular structures (Bennett and Lorenzo, 2013). Importantly, the intracellular localization of the ankG CTer domain was resistant to cytoskeleton perturbations. A short-term high-KCl treatment that started to disassemble the AIS could alter the βIV-spectrin periodic lattice, but not the radial extent of ankG. These nanoscale features of the AIS scaffold may thus be essential for the stability of the AIS as a compartment.

Molecular Organization of ankG Hints at Its Role in Regulating Protein Transport through the AIS

The "dendrification" of the proximal axon observed after ankG depletion (Hedstrom et al., 2008; Sobotzik et al., 2009) led to

(E and F) Same as (A) and (B) for an AIS labeled for Nav channels (green) and βIV-spectrin SD (magenta).
(G and H) Same as (A) and (B) for an AIS labeled for ankG SB (green) and βIV-spectrin SD (magenta).
(I and J) Same as (A) and (B) for an AIS labeled for ankG CTer (green) and βIV-spectrin SD (magenta).
(K and L) Same as (A) and (B) for an AIS labeled for ankG tail480 (green) and ankG CTer (magenta).
(M) Radial distance to βIV-spectrin SD for the α-tubulin, neurofascin, Nav, ankG SB, and ankG CTer labeling. Red line is βIV-spectrin SD reference at 0 nm (n = 284–832 profiles; N = 2–9).
(N) Radial distance between the ankG CTer and the ankG tail480 labeling (shifted Y scale to align with the βIV-spectrin SD reference in K; n = 168; N = 2).
(O) Structural model of the AIS radial organization.
See also Figure S5.

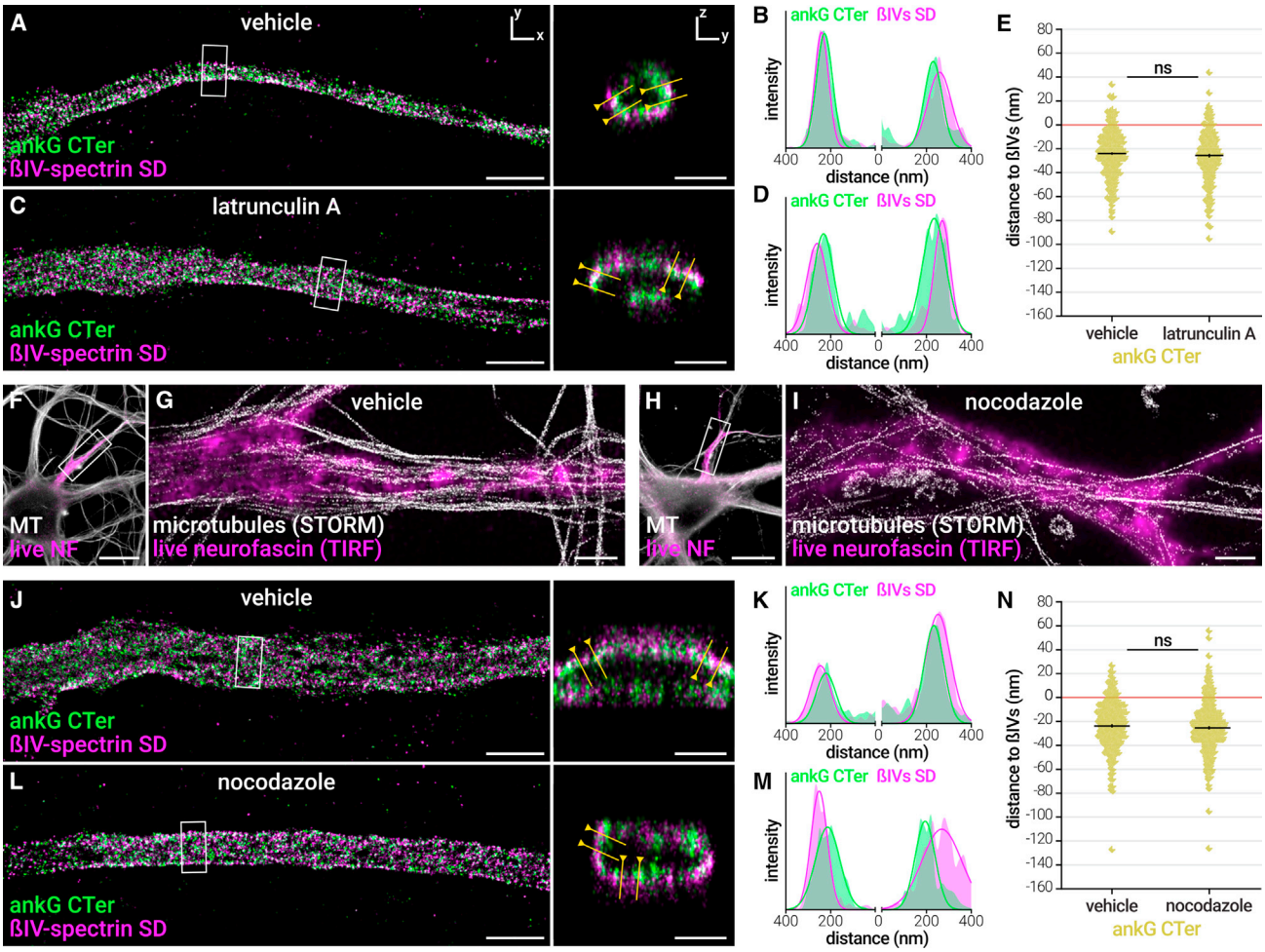

Figure 5. The Radial Extent of ankG Is Resistant to Actin or Microtubule Perturbation

(A) 3D-STORM image of the AIS from a neuron treated with vehicle (0.1% DMSO; 1 hr), fixed and labeled for ankG CTer (green) and ßIV-spectrin SD (magenta). The scale bars for (A), (C), (G), (I), (J), and (L) represent 2 μm for XY image and 0.5 μm for YZ section.

(B) Intensity profiles for each channel along the yellow line.

(C and D) Same as (A) and (B) for an AIS from a sister culture treated with latrunculin A (latA; 5 μM; 1 hr).

(E) Radial distance to ßIV-spectrin SD for the ankG CTer labeling in vehicle- and latA-treated neurons (n = 225–289 profiles; N = 3).

(F) Epifluorescence image of a neuron treated with vehicle (0.1% DMSO; 3 hr), labeled live for neurofascin (NF) (magenta), fixed/extracted, and labeled for microtubules (gray).

(G) Overlay of a STORM images of the microtubule labeling (gray) with a scaled TIRF image of the live neurofascin labeling (magenta) along the AIS shown in (F).

(H and I) Same as (F) and (G) for an AIS from a sister culture treated with nocodazole (20 μM; 3 hr).

(J and K) 3D-STORM image (J) of the AIS from a neuron treated with vehicle, fixed, and labeled for ankG CTer (green) and ßIV-spectrin SD (magenta); (K) corresponding intensity profiles.

(L and M) Same as (J) and (K) for an AIS from a sister culture treated with nocodazole.

(N) Radial distance to ßIV-spectrin SD for the ankG CTer labeling in vehicle- and nocodazole-treated neurons (n = 300–346; N = 3).

See also Figure S6.

propose a role for the AIS in the maintenance of axonal identity via a diffusion barrier and an intracellular filter (Leterrier and Dargent, 2014; Rasband, 2010). Since its initial description (Song et al., 2009), the existence of an intracellular filter in the AIS that regulates protein traffic between the soma and axon has been a debated issue (Petersen et al., 2014; Watanabe et al., 2012). How ankG could participate in the regulation of protein transport into the axon remains unknown, as ankG has been primarily detected near the plasma membrane by immunogold electron microscopy (Iwakura et al., 2012; Le Bras et al., 2013). Even if ankG forms ~150-nm-long rods (Jones et al., 2014), our results show that it reaches depths within ~50 nm of the plasma membrane, ruling out a fully radial orientation and the hypothesis of ankG extending through the axoplasm to reach deep intracellular targets (Davis et al., 1996; Leterrier and Dargent, 2014). The shallow depth reached by ankG in our study suggests that the AIS scaffold could rather recruit and spatially organize a population of

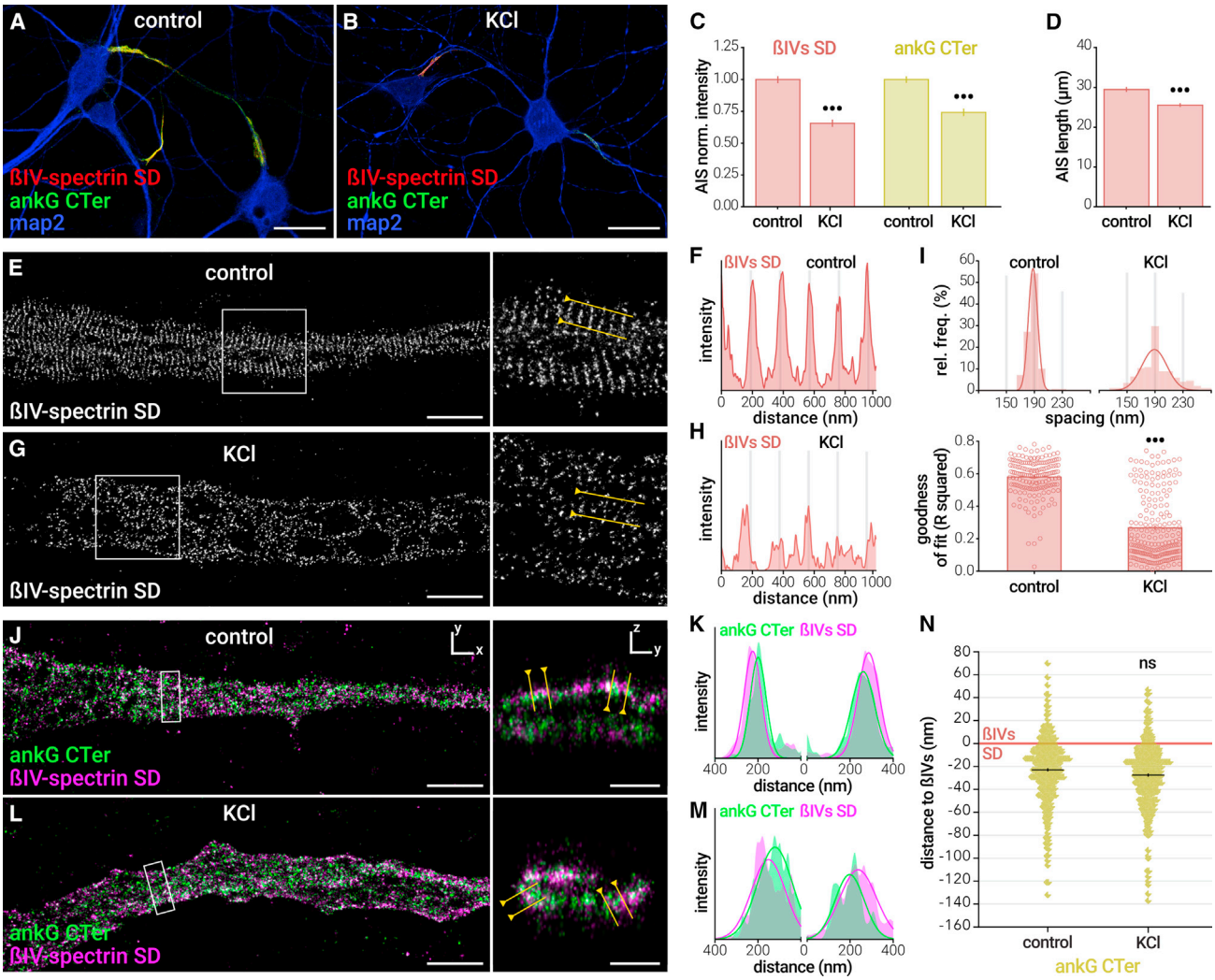

Figure 6. Elevated K+ Partially Disassembles the AIS and Impairs the Periodic Lattice, but Not the ankG Radial Extent

(A and B) Deconvolved epifluorescence images of neurons untreated (A; control medium 5 mM KCl) or incubated with elevated K+ (B; 45 mM KCl; 3 hr), fixed and stained for ßIV-spectrin SD (red), ankG CTer (green), and map2 (blue). The scale bars represent 20 µm.

(C) Labeling intensity at the AIS of neurons for ßIV-spectrin SD (red, left) and ankG CTer (green, right), normalized to the vehicle condition.

(D) AIS length measured on the ßIV-spectrin SD labeling (for C and D, n = 103–126 AIS; N = 3 or 4).

(E) STORM image of AIS from control neurons labeled for ßIV-spectrin SD. The scale bars for (E), (G), (J), and (L) represent 2 µm for XY images and 0.5 µm for YZ sections.

(F) Intensity profile along the yellow line.

(G and H) Same as (E) and (F) for an AIS from a sister culture treated with KCl (images and intensity profiles are identically processed for both conditions).

(I) (Top) Histogram of the spacing values in the control and KCl conditions. (Bottom) Goodness of sinusoid fit (R squared) for the ßIV-spectrin SD labeling for control or KCl-treated neurons is shown (for both graphs, n = 130–206 profiles; N = 3 or 4).

(J) 3D-STORM image of the AIS from control neurons, fixed and labeled for ankG CTer (green) and ßIV-spectrin SD (magenta).

(K) Intensity profiles for each channel along the yellow lines.

(L and M) Same as (J) and (K) for an AIS from a sister culture treated with KCl.

(N) Radial distance to ßIV-spectrin SD for the ankG CTer labeling in control and KCl-treated neurons (n = 415–431; N = 3).

microtubules close to the axolemma (Westrum and Gray, 1976). This specific microtubule organization could in turn influence polarized traffic to and from the axon, explaining how the AIS participate in the sorting of vesicular trafficking. Interestingly, a recently identified giant ankG isoform organizes the distribution of microtubules along the axon in *Drosophila* neurons (Stephan et al., 2015).

The AIS: From Cellular Traffic to Brain and Nervous System Disorders

In conclusion, we show that the AIS scaffold is a precisely organized compartment, with a longitudinal periodicity and a radial layering. This nanoscale organization is robust, pointing to its potential importance for proper cell function. Our work confirms the strength of super-resolution microscopy for elucidating the

architecture of neuronal assemblies, down to the macromolecular level (Maglione and Sigrist, 2013). Knowledge of the AIS nanoscale architecture will help decipher the molecular mechanisms that underpin neuronal excitability and protein mobility in polarized cells. Beyond this fundamental relevance, understanding the AIS structure and function has neuro-pathological implications. AnkG gene variants and mutations have been consistently associated with in several neuropsychiatric disorders, including bipolar disorders and schizophrenia (Iqbal et al., 2013; Leussis et al., 2012). Furthermore, affected axonal transport is a key factor in most neurodegenerative diseases, where the gatekeeper function of the AIS was recently implicated (Sun et al., 2014). Our structural work will hopefully open the way to a better understanding of the AIS crucial functions, in physiological as well as pathological contexts.

EXPERIMENTAL PROCEDURES

Antibodies and Reagents

Rabbit polyclonal anti-ßIV-spectrin antibodies were gifts from Matthew Rasband (Baylor College of Medicine). Rabbit polyclonal anti-480-kDa ankG (residues 3,516–3,530 of human 480-kDa ankG) was a gift from François Couraud (Université Pierre et Marie Curie). For two-color STORM, paired fluorophore-conjugated secondary antibodies were made by coupling unconjugated antibodies with reactive activator and reporter fluorophores, according to the N-STORM sample preparation protocol (Nikon Instruments).

Animals and Neuronal Cultures

The use of Wistar rats followed the guidelines established by the European Animal Care and Use Committee (86/609/CEE) and was approved by the local ethics committee (agreement D13-055-8). Rat hippocampal neurons were cultured on 18-mm coverslips at a density of 6,000/cm^2 following the Banker method, above a feeder glia layer in B27-supplemented medium (Kaech and Banker, 2006).

Immunocytochemistry and STORM Imaging

After 14–21 days in culture, neurons were fixed using 4% PFA or using an extraction-fixation method optimized for microtubule labeling. After blocking, they were incubated with primary antibodies overnight at 4°C and then with secondary antibodies for 1 hr at room temperature. STORM imaging was performed on an N-STORM microscope (Nikon Instruments). Coverslips were imaged in STORM buffer: Tris 50 mM (pH 8); NaCl 10 mM; 10% glucose; 100 mM MEA; 3.5 U/ml pyranose oxidase; and 40 μg/ml catalase. For single-color imaging, the sample was continuously illuminated at 647 nm (full power) and 30,000–60,000 images were acquired at 67 Hz, with progressive reactivation by simultaneous 405-nm illumination. Two-color STORM imaging was either performed by successive imaging with 488- and 647-nm lasers (for double staining comprising phalloidin-Atto 488) or using alternated sequences of one activator frame followed by three reporter frames. The N-STORM software (Nikon Instruments) was used for the localization of single fluorophores.

Image Processing and Analysis

Image reconstructions were performed using the ThunderSTORM ImageJ plugin (Ovesný et al., 2014). Custom scripts and macros were used to automate images reconstructions. For quantification of longitudinal periodicity, intensity profiles were fitted using a sinusoid function. The histogram of spacing values was fitted with a Gaussian curve to obtain the mean spacing and spread. For quantification of radial distributions, radial profiles were obtained on YZ transverse projections and the distance between epitopes defined as the difference between the maxima of Gaussian fits on each channel. For quantification of the AIS length and components intensity on epifluorescence images, a threshold was applied on line profiles along the axon to detect the AIS position (Grubb and Burrone, 2010b). Significances were tested using two-tailed unpaired t tests (two conditions) or one-way ANOVA followed by Tukey posttest (three or more conditions). In all figures and tables, significance is coded as ns, non-significant; *$p < 0.05$; **$p < 0.01$; and ***$p < 0.001$.

SUPPLEMENTAL INFORMATION

Supplemental Information includes Supplemental Experimental Procedures, six figures, and two tables and can be found with this article online at http://dx.doi.org/10.1016/j.celrep.2015.11.051.

AUTHOR CONTRIBUTIONS

C.L., conception and design, acquisition of data, analysis and interpretation of data, drafting or revising the article; J.P., acquisition of data, analysis and interpretation of data; G.C., acquisition of data; C.D., acquisition of data; F.R.B., contributed essential data or reagents; B.D., conception and design, interpretation of data, drafting or revising the article.

ACKNOWLEDGMENTS

We thank M. Rasband, V. Bennett, and F. Couraud for providing antibodies and plasmids. We also would like to thank D. Choquet and J.-B. Sibarita for insightful discussions; D. Marguet, S. Mailfert, M. Mondin, and J. Petersen for their help during the initial stages of this study; S. Bezin at Nikon Instruments and M.-P. Blanchard at CRN2M imaging facility for their assistance; and S. Roy, F. Castets, and M.-J. Papandreou for discussions and careful reading of the manuscript. This work was supported by a grant to B.D. from the French Agence Nationale de la Recherche (ANR-2011-BSV4-001-1).

Received: July 16, 2015
Revised: October 14, 2015
Accepted: November 13, 2015
Published: December 17, 2015

REFERENCES

Bennett, V., and Lorenzo, D.N. (2013). Spectrin- and ankyrin-based membrane domains and the evolution of vertebrates. Curr. Top. Membr. *72*, 1–37.

Bennett, V., Davis, J., and Fowler, W.E. (1982). Brain spectrin, a membrane-associated protein related in structure and function to erythrocyte spectrin. Nature *299*, 126–131.

Bréchet, A., Fache, M.-P., Brachet, A., Ferracci, G., Baude, A., Irondelle, M., Pereira, S., Leterrier, C., and Dargent, B. (2008). Protein kinase CK2 contributes to the organization of sodium channels in axonal membranes by regulating their interactions with ankyrin G. J. Cell Biol. *183*, 1101–1114.

D'Este, E., Kamin, D., Göttfert, F., El-Hady, A., and Hell, S.W. (2015). STED nanoscopy reveals the ubiquity of subcortical cytoskeleton periodicity in living neurons. Cell Rep. *10*, 1246–1251.

Davis, J.Q., Lambert, S., and Bennett, V. (1996). Molecular composition of the node of Ranvier: identification of ankyrin-binding cell adhesion molecules neurofascin (mucin+/third FNIII domain-) and NrCAM at nodal axon segments. J. Cell Biol. *135*, 1355–1367.

Grubb, M.S., and Burrone, J. (2010a). Building and maintaining the axon initial segment. Curr. Opin. Neurobiol. *20*, 481–488.

Grubb, M.S., and Burrone, J. (2010b). Activity-dependent relocation of the axon initial segment fine-tunes neuronal excitability. Nature *465*, 1070–1074.

Hedstrom, K.L., Xu, X., Ogawa, Y., Frischknecht, R., Seidenbecher, C.I., Shrager, P., and Rasband, M.N. (2007). Neurofascin assembles a specialized extracellular matrix at the axon initial segment. J. Cell Biol. *178*, 875–886.

Hedstrom, K.L., Ogawa, Y., and Rasband, M.N. (2008). AnkyrinG is required for maintenance of the axon initial segment and neuronal polarity. J. Cell Biol. *183*, 635–640.

Iqbal, Z., Vandeweyer, G., van der Voet, M., Waryah, A.M., Zahoor, M.Y., Besseling, J.A., Roca, L.T., Vulto-van Silfhout, A.T., Nijhof, B., Kramer, J.M., et al. (2013). Homozygous and heterozygous disruptions of ANK3: at the crossroads

of neurodevelopmental and psychiatric disorders. Hum. Mol. Genet. *22*, 1960–1970.

Iwakura, A., Uchigashima, M., Miyazaki, T., Yamasaki, M., and Watanabe, M. (2012). Lack of molecular-anatomical evidence for GABAergic influence on axon initial segment of cerebellar Purkinje cells by the pinceau formation. J. Neurosci. *32*, 9438–9448.

Jaworski, J., Kapitein, L.C., Gouveia, S.M., Dortland, B.R., Wulf, P.S., Grigoriev, I., Camera, P., Spangler, S.A., Di Stefano, P., Demmers, J., et al. (2009). Dynamic microtubules regulate dendritic spine morphology and synaptic plasticity. Neuron *61*, 85–100.

Jenkins, S.M., and Bennett, V. (2001). Ankyrin-G coordinates assembly of the spectrin-based membrane skeleton, voltage-gated sodium channels, and L1 CAMs at Purkinje neuron initial segments. J. Cell Biol. *155*, 739–746.

Jenkins, P.M., Kim, N., Jones, S.L., Tseng, W.-C., Svitkina, T.M., Yin, H.H., and Bennett, V. (2015). Giant ankyrin-G: a critical innovation in vertebrate evolution of fast and integrated neuronal signaling. Proc. Natl. Acad. Sci. USA *112*, 957–964.

Jones, S.L., Korobova, F., and Svitkina, T. (2014). Axon initial segment cytoskeleton comprises a multiprotein submembranous coat containing sparse actin filaments. J. Cell Biol. *205*, 67–81.

Kaech, S., and Banker, G. (2006). Culturing hippocampal neurons. Nat. Protoc. *1*, 2406–2415.

Kapitein, L.C., and Hoogenraad, C.C. (2011). Which way to go? Cytoskeletal organization and polarized transport in neurons. Mol. Cell. Neurosci. *46*, 9–20.

Lacas-Gervais, S., Guo, J., Strenzke, N., Scarfone, E., Kolpe, M., Jahkel, M., De Camilli, P., Moser, T., Rasband, M.N., and Solimena, M. (2004). BetaIV-Sigma1 spectrin stabilizes the nodes of Ranvier and axon initial segments. J. Cell Biol. *166*, 983–990.

Le Bras, B., Fréal, A., Czarnecki, A., Legendre, P., Bullier, E., Komada, M., Brophy, P.J., Davenne, M., and Couraud, F. (2013). In vivo assembly of the axon initial segment in motor neurons. Brain Struct. Funct. *219*, 1433–1450.

Leterrier, C., and Dargent, B. (2014). No Pasaran! Role of the axon initial segment in the regulation of protein transport and the maintenance of axonal identity. Semin. Cell Dev. Biol. *27*, 44–51.

Leterrier, C., Vacher, H., Fache, M.-P., d'Ortoli, S.A., Castets, F., Autillo-Touati, A., and Dargent, B. (2011). End-binding proteins EB3 and EB1 link microtubules to ankyrin G in the axon initial segment. Proc. Natl. Acad. Sci. USA *108*, 8826–8831.

Leussis, M.P., Madison, J.M., and Petryshen, T.L. (2012). Ankyrin 3: genetic association with bipolar disorder and relevance to disease pathophysiology. Biol. Mood Anxiety Disord. *2*, 18.

Lorenzo, D.N., Badea, A., Davis, J., Hostettler, J., He, J., Zhong, G., Zhuang, X., and Bennett, V. (2014). A PIK3C3-ankyrin-B-dynactin pathway promotes axonal growth and multiorganelle transport. J. Cell Biol. *207*, 735–752.

Maglione, M., and Sigrist, S.J. (2013). Seeing the forest tree by tree: super-resolution light microscopy meets the neurosciences. Nat. Neurosci. *16*, 790–797.

Nakada, C., Ritchie, K., Oba, Y., Nakamura, M., Hotta, Y., Iino, R., Kasai, R.S., Yamaguchi, K., Fujiwara, T., and Kusumi, A. (2003). Accumulation of anchored proteins forms membrane diffusion barriers during neuronal polarization. Nat. Cell Biol. *5*, 626–632.

Normand, E.A., and Rasband, M.N. (2015). Subcellular patterning: axonal domains with specialized structure and function. Dev. Cell *32*, 459–468.

Ovesný, M., Křížek, P., Borkovec, J., Svindrych, Z., and Hagen, G.M. (2014). ThunderSTORM: a comprehensive ImageJ plug-in for PALM and STORM data analysis and super-resolution imaging. Bioinformatics *30*, 2389–2390.

Petersen, J.D., Kaech, S., and Banker, G. (2014). Selective microtubule-based transport of dendritic membrane proteins arises in concert with axon specification. J. Neurosci. *34*, 4135–4147.

Rasband, M.N. (2010). The axon initial segment and the maintenance of neuronal polarity. Nat. Rev. Neurosci. *11*, 552–562.

Redmond, L., Kashani, A.H., and Ghosh, A. (2002). Calcium regulation of dendritic growth via CaM kinase IV and CREB-mediated transcription. Neuron *34*, 999–1010.

Schafer, D.P., Jha, S., Liu, F., Akella, T., McCullough, L.D., and Rasband, M.N. (2009). Disruption of the axon initial segment cytoskeleton is a new mechanism for neuronal injury. J. Neurosci. *29*, 13242–13254.

Sobotzik, J.-M., Sie, J.M., Politi, C., Del Turco, D., Bennett, V., Deller, T., and Schultz, C. (2009). AnkyrinG is required to maintain axo-dendritic polarity in vivo. Proc. Natl. Acad. Sci. USA *106*, 17564–17569.

Song, A.-H., Wang, D., Chen, G., Li, Y., Luo, J., Duan, S., and Poo, M.-M. (2009). A selective filter for cytoplasmic transport at the axon initial segment. Cell *136*, 1148–1160.

Stephan, R., Goellner, B., Moreno, E., Frank, C.A., Hugenschmidt, T., Genoud, C., Aberle, H., and Pielage, J. (2015). Hierarchical microtubule organization controls axon caliber and transport and determines synaptic structure and stability. Dev. Cell *33*, 5–21.

Sun, X., Wu, Y., Gu, M., Liu, Z., Ma, Y., Li, J., and Zhang, Y. (2014). Selective filtering defect at the axon initial segment in Alzheimer's disease mouse models. Proc. Natl. Acad. Sci. USA *111*, 14271–14276.

Uemoto, Y., Suzuki, S., Terada, N., Ohno, N., Ohno, S., Yamanaka, S., and Komada, M. (2007). Specific role of the truncated betaIV-spectrin Sigma6 in sodium channel clustering at axon initial segments and nodes of ranvier. J. Biol. Chem. *282*, 6548–6555.

Watanabe, K., Al-Bassam, S., Miyazaki, Y., Wandless, T.J., Webster, P., and Arnold, D.B. (2012). Networks of polarized actin filaments in the axon initial segment provide a mechanism for sorting axonal and dendritic proteins. Cell Rep. *2*, 1546–1553.

Westrum, L.E., and Gray, E.G. (1976). Microtubules and membrane specializations. Brain Res. *105*, 547–550.

Winckler, B., Forscher, P., and Mellman, I. (1999). A diffusion barrier maintains distribution of membrane proteins in polarized neurons. Nature *397*, 698–701.

Xu, K., Zhong, G., and Zhuang, X. (2013). Actin, spectrin, and associated proteins form a periodic cytoskeletal structure in axons. Science *339*, 452–456.

Yang, Y., Ogawa, Y., Hedstrom, K.L., and Rasband, M.N. (2007). betaIV spectrin is recruited to axon initial segments and nodes of Ranvier by ankyrinG. J. Cell Biol. *176*, 509–519.

Zhong, G., He, J., Zhou, R., Lorenzo, D., Babcock, H.P., Bennett, V., and Zhuang, X. (2014). Developmental mechanism of the periodic membrane skeleton in axons. eLife *3*, e04581.